Nano Research 2015, 8(5): 1595–1603
DOI 10.1007/s12274-014-0648-z
Research Article
ISSN 1998-0124
CN 11-5974/O4

Aerosol-assisted rapid synthesis of SnS-C composite microspheres as anode material for Na-ion batteries

Seung Ho Choi and Yun Chan Kang (✉)

Department of Materials Science and Engineering, Korea University, Anam-Dong, Seongbuk-Gu, Seoul 136-713, Republic of Korea

Received: 2 October 2014
Revised: 14 November 2014
Accepted: 19 November 2014

KEYWORDS
tin sulfide,
anode material,
carbon composite,
sodium battery,
energy storage

ABSTRACT

SnS-C composite powders were prepared through one-pot spray pyrolysis for use as anode materials for Na-ion batteries. C microspheres with uniformly attached cubic-like SnS nanocrystals, which have an amorphous C coating layer, were formed at a preparation temperature of 900 ˚C. The initial discharge capacities of the bare SnS and SnS-C composite powders at a current density of 500 mA·g^{-1} were 695 and 740 mA·h·g^{-1}, respectively. The discharge capacities after 50 cycles and the capacity retentions measured from the second cycle of the bare SnS and SnS-C composite powders were 25 and 433 mA·h·g^{-1} and 5 and 89%, respectively. The prepared SnS-C composite powders with high reversible capacities and good cycle performance can be used as Na-ion battery anode materials.

1 Introduction

Na-ion batteries (NIBs) are possibly the next-generation of rechargeable batteries for large-scale energy storage and can potentially replace lithium-ion batteries (LIBs) because of the natural abundance of Na resources [1–9]. NIBs operate under a similar working principle as LIBs because of the analogous storage behavior in Na and Li ions [1–9]. Therefore, various types of materials that were developed for LIBs have also been tested as electrode materials for NIBs [10–17]. However, the successful use of these electrode materials in LIBs has not been replicated in NIBs. The cell potentials, in particular, of most transition metal oxides in the discharge process shift to lower values after the insertion of Na^+ ions [9–17]. This shift, in turn, hinders the attainment of sufficient electrochemical decomposition.

Sn-based materials, such as Sn metal, SnO_2, SnS, and SnS_2, have been extensively studied as anode materials for LIBs and NIBs because of their high theoretical Li-ion storage capacities [18–39]. SnO_2-based materials can deliver a reversible theoretical capacity of 894 mA·h·g^{-1} by forming the $Li_{15}Sn_4$ alloy [18–24]. In the LIB system, the plateau at approximately 0.8 V of SnO_2 materials in their first discharge process

Address correspondence to yckang@korea.ac.kr

is related to sufficient electrochemical decomposition of SnO_2 for the Li-ion storage process. However, SnO_2 materials in NIBs have difficulty attaining sufficient electrochemical decomposition because the cell potentials of the metal oxide electrodes shift (by approximately 0.8 V) to lower values when Li is substituted by Na in conversion reactions [9]. In the first discharge step, SnS and SnS_2 materials, unlike SnO_2, exhibit higher initial plateau values (approximately 0.7 V) for electrochemical decomposition and are, therefore, promising candidates for use as Na-ion battery anode materials [32–38]. However, SnS exhibited low reversible capacities and poor cycle life because of the larger Na-ion radius, slower reaction kinetics, and large volume expansion from Na-ion insertion.

Sn-based nanomaterials of various structures have been studied to improve their capacities and cycling performance for Na-ion storage [10, 32–39]. Sn-based C and graphene composite materials have also been studied for Na-ion storage [32–39]. The inclusion of C materials improves the structural stability of these Sn-based composites during cycling and augments the conductance of the active materials. SnS-C composite materials prepared primarily by liquid solution methods have exhibited good electrochemical properties for Na-ion storage. Zhou *et al.* reported that SnS-graphene hybrid nanostructured composites were observed to have an excellent specific capacity of 492 $mA{\cdot}h{\cdot}g^{-1}$ after 250 cycles at a current density of 810 $mA{\cdot}g^{-1}$ [34]. Qu *et al.* reported that the SnS_2-reduced graphene-oxide hybrid structures prepared by hydrothermal processing also exhibit excellent Na^+ storage properties [35].

Spray pyrolysis with a fast synthesis time has been applied in the preparation of metal sulfide-C composite microspheres for LIB applications; however, SnS-C composite materials for Li- or Na-ion storage have not been prepared using this technique [40, 41]. Therefore, in this study, C microspheres with uniformly attached SnS nanocrystals were prepared using a simple one-pot spray pyrolysis process. The formation mechanism and Na-ion storage properties of the resulting SnS-C composite powders were investigated.

2 Experimental

2.1 Synthesis of SnS-C composite powders

SnS-C composite powders were prepared directly using spray pyrolysis from an aqueous spray solution. Figure S1 presents a schematic of the ultrasonic spray pyrolysis system that was used to prepare the SnS-C composite. A 1,200 mm × 50 mm (length × diameter) quartz reactor was used in the preparation. The reactor temperature was maintained at 900 ℃, and the flow rate of the 10% H_2/Ar carrier gas was 5 $L{\cdot}min^{-1}$. An aqueous spray solution was prepared from tin oxalate (SnC_2O_4, Sigma-Aldrich) and thiourea (CH_4N_2S, Junsei). Polyvinyl polyrridone (PVP) (M_w = 45,000) was used as the C source material to form the C composite powders. Then, 3.0 g of SnC_2O_4, 10 g of CH_4N_2S, and 3.5 g of PVP were dissolved in 250 mL of distilled water. Bare SnS powders were also prepared using one-pot spray pyrolysis from the aqueous spray solution without PVP.

2.2 Characterization

The crystal structures of the powders were investigated by X-ray diffraction (XRD, X'Pert PRO MPD) using Cu Kα radiation (λ = 1.5418 Å). The morphological characteristics were investigated using high-resolution scanning electron microscopy (FE-SEM, Hitachi S-4800) and high-resolution transmission electron microscopy (HR-TEM, JEOL JEM-2100F). An accelerating voltage of 200 kV was used for HR-TEM. The specific surface areas of the microspheres were calculated from a Brunauer–Emmett–Teller (BET) analysis of nitrogen adsorption measurements (TriStar 3000). The microspheres were also investigated using X-ray photoelectron spectroscopy (XPS, ESCALAB-210) with Al Kα radiation (1486.6 eV). Thermal gravimetric analysis (TGA, SDT Q600) was performed in air at a heating rate of 10 ℃$\cdot min^{-1}$ to determine the amount of C in the microspheres.

2.3 Electrochemical measurements

The capacities and cycle properties of the powders were determined using a 2032-type coin cell. The electrode was prepared from a mixture containing 70 wt% active material, 20 wt% Super P, and 10 wt%

sodium carboxymethyl cellulose (CMC) binder. Stick-type Na metal and a microporous polypropylene film were used as the counter electrode and separator, respectively. The electrolyte consisted of a solution of 1 M $NaClO_4$ (Aldrich) in a 1:1 volume mixture of ethylene carbonate/dimethyl carbonate (EC/DMC) to which 5 wt% fluoroethylene carbonate (FEC) was added. The charge–discharge characteristics of the samples were determined by cycling the potential in the range of 0.001–3.0 V at fixed current densities. The corresponding cyclic voltammetry (CV) was performed at a scan rate of 0.1 $mV \cdot s^{-1}$. The dimensions of the negative electrode were 1 cm × 1 cm, and the active mass loading was approximately 1.2 $mg \cdot cm^{-2}$. The capacities of this study were based on the total weight of the SnS-C composite. Electrochemical impedance spectroscopy (EIS) was performed using a ZIVE SP1 over a frequency range of 0.01–100 kHz.

3 Results and discussion

Bare SnS and SnS-C composite powders were prepared using one-pot spray pyrolysis from the spray solutions with and without PVP as the C source material. The crystal structures of the powders are shown in Fig. 1. As the XRD pattern reveals, the SnS powders prepared at 900 ℃ without PVP had primarily an orthorhombic crystal structure with small impurity phases of SnO and SnO_2. However, the SnS-C composite powders prepared at 700 and 900 ℃ had phase pure orthorhombic SnS crystal structures. During spray pyrolysis, SnO powder forms as an intermediate product of the decomposition of SnC_2O_4, which occurs in the front part of the reactor that is maintained at 900 ℃. In addition, the H_2S gas, formed by the decomposition of CH_4N_2S, enhances the reducing atmosphere induced by the 10%-H_2/Ar-reducing carrier gas surrounding the powders. The SnO is reduced to Sn metal during sulfidation of the powders in the rear part of the reactor, resulting in the formation of SnS. The micron size and dense structure of the powders retard the reduction of SnO and sulfidation into SnS. Therefore, the SnS powders with SnO and SnO_2 impurities were prepared by one-pot spray pyrolysis from the spray solution without PVP. The SnO-C composite powder was formed as an intermediate product in the front part of the reactor maintained at temperatures of 700 or 900 ℃ because of the decomposition of SnC_2O_4 and carbonization of PVP. The C component enhances the reducing atmosphere around the SnO-C composite powders but also minimizes the crystal growth of the SnO. Ultrafine SnO nanocrystals are uniformly dispersed within the SnO-C composite powder. The ultrafine SnO nanocrystals were rapidly reduced to Sn nanocrystals during the sulfidation process in the rear part of the reactor. Therefore, SnS-C composite powders with the phase pure crystal structure of orthorhombic SnS were prepared by one-pot spray pyrolysis even at a low preparation temperature of 700 ℃. The powders were held for 6 s inside the reactor that was maintained at this temperature.

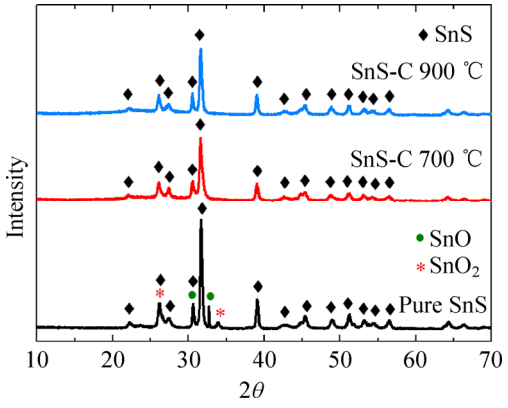

Figure 1 XRD patterns of the bare SnS and SnS-C composite microspheres prepared using one-pot spray pyrolysis.

The morphologies of the bare SnS powders with SnO and SnO_2 impurities are shown in Fig. 2. The SEM and TEM images reveal the cubic-like structure of the bare SnS powders. In general, one spherical ceramic powder with a hollow or dense structure was formed from each droplet in the spray pyrolysis. In this study, one SnS powder was also formed from one droplet by the drying and sulfidation processes. The morphology of the powders, however, was changed by melting of SnS, which has a melting temperature of 882 ℃. Therefore, rapid crystallization of the melted powder in the outlet part of the reactor maintained at 900 ℃ resulted in the plate-like structure observed. Plate-like powders were also observed in the FE-SEM and TEM images. Some powders consisted of stacked structures of the nanoplates; these loosely stacked nanoplates separated into several individual plates during preparation of the bare SnS powders. The

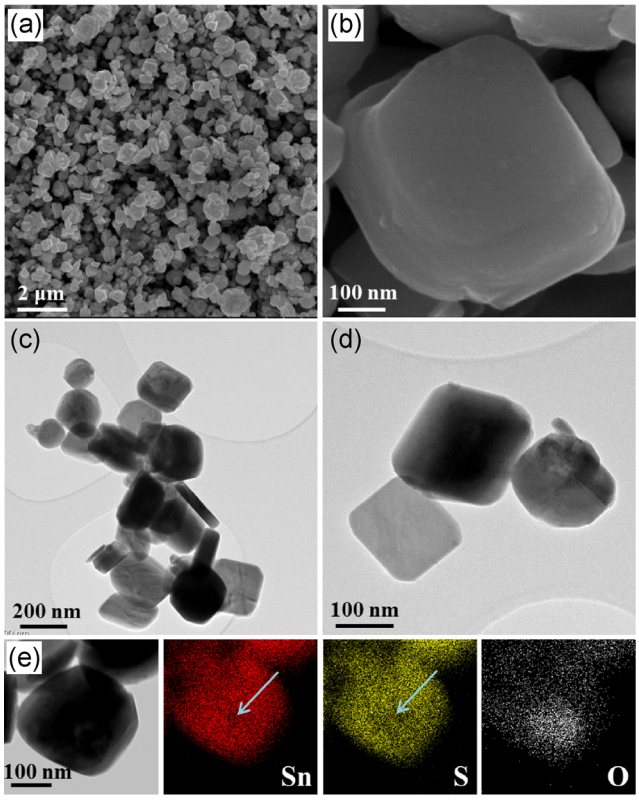

Figure 2 Morphologies and elemental mapping images of the bare SnS nanoplates prepared at 900 ˚C: (a) and (b) FE-SEM images; (c) and (d) TEM images; and (e) elemental mapping images of Sn, S, and O components.

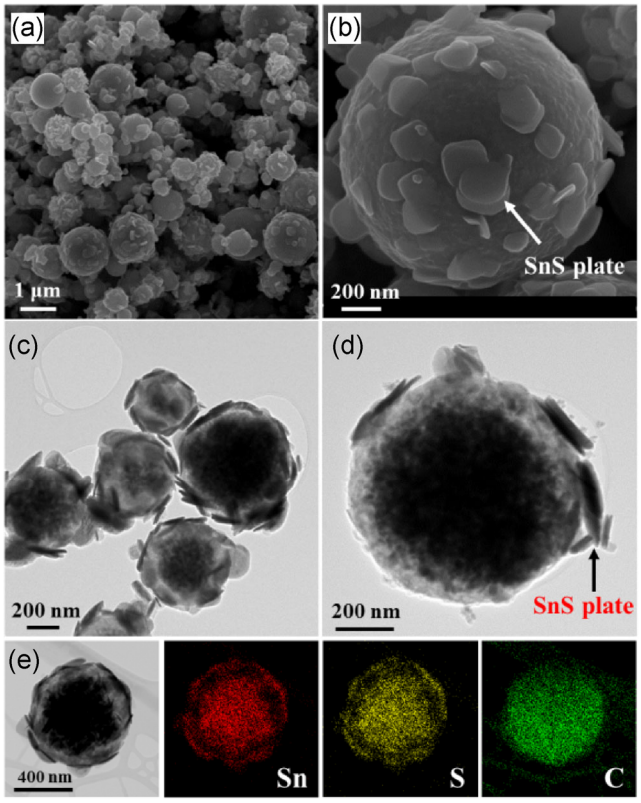

Figure 3 Morphologies and elemental mapping images of the SnS-C microspheres prepared at 700 ˚C: (a) and (b) FE-SEM images; (c) and (d) TEM images; and (e) elemental mapping images of Sn, S, and C components.

elemental mapping images of the powders, presented in Fig. 2(e), reveal that Sn is uniformly distributed in the powder. However, the S and O components are mainly located on the outside and inside, respectively. In addition, a void was observed in the elemental mapping images, as indicated by the arrows in Fig. 2(e). The melting of the SnO part did not occur due to the incomplete sulfidation process of the powder.

The morphologies of the SnS-C composite powders with the phase pure crystal structure of orthorhombic SnS prepared at temperatures of 700 and 900 ˚C are shown in Figs. 3 and 4. The SnS-C composite powders had hierarchical structures irrespective of the preparation temperature. Preparation at 700 ˚C resulted in powders with spherical morphology decorated with nanoplates, as observed in Fig. 3. The nanoplates separated from the spherical powder are also observed in the TEM images in Figs. 3(c) and 3(d). Some of the nanoplates that were loosely attached to the surface of the spherical powders were removed during ultrasonic vibration for the preparation of the TEM samples. Further characterization by elemental mapping (Fig. 3(e)) revealed that Sn and S are both deficient in the surface layer, whereas the C component is uniformly distributed in the powder. The TEM and elemental mapping images also revealed that the ultrafine SnS nanocrystals are uniformly distributed in the inner part of the composite powder. However, the SnS nanoplates, which were formed during the sulfidation process, clustered the Sn component around the surface of the powder. The SnS-C composite powders prepared at 900 ˚C had different morphologies than those produced at 700 ˚C. Preparation at 900 ˚C resulted in the formation of cubic-like nanocrystals that were several tens of nanometers in size, which were uniformly attached to the spherical powders (Fig. 4). Elemental mapping revealed the attached SnS nanocrystals around the surface of the spherical C powder (Fig. 4(e)). Moreover, growth of the nanocrystals was initiated on the surface of the composite

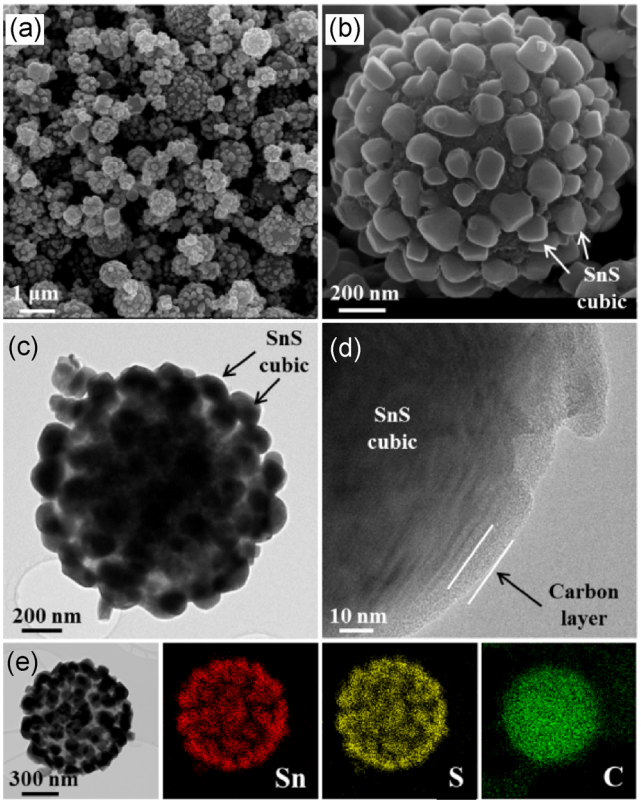

Figure 4 Morphologies and elemental mapping images of the SnS-C microspheres prepared at 900 ˚C: (a) and (b) FE-SEM images; (c) and (d) TEM images; and (e) elemental mapping images of Sn, S, and C components.

powder by consuming the ultrafine SnS nanocrystals embedded within the C sphere. In other words, Ostwald ripening resulted in uniform attachment of cubic-like SnS nanocrystals with an amorphous C coating layer to the C microspheres. The amorphous C layer around the cubic-like SnS nanocrystals had a thickness of 8 nm (Fig. 2(d)). Scheme 1 presents a schematic of the detailed formation mechanism of the SnS-C composite powder in the spray pyrolysis process.

The thermogravimetric (TG) curves of the SnS-C composite powders are shown in Fig. S2 and reveal a distinct decrease in weight at approximately 400 ˚C because of the decomposition of the C material. The C contents of the SnS-C composite powders prepared at 700 and 900 ˚C were 40 and 25%, respectively. The slight weight increase at approximately 370 ˚C in the TG curve of the composite powders prepared at 900 ˚C indicated the existence of a small impurity of Sn metal. The BET surface area of the SnS-C composite powders prepared at 900 ˚C was 5 $m^2 \cdot g^{-1}$. To confirm the detailed characteristics of the SnS-C composite powders prepared at 900 ˚C, XPS analysis of the powders was performed, and the results are presented in Fig. S3. Two strong Sn3d XPS peaks at approximately 486.7 and 495.1 eV, which can be attributed to the $Sn3d_{5/2}$ and $Sn3d_{3/2}$ binding energies of SnS, are observed [42, 43]. The peak at 161.4 eV in Fig. S3(b) can be indexed as the S2p peak of SnS [42, 43]. The C1s XPS peak observed at 284.6 eV in Fig. S3(c) represents the binding energy of the sp^2 C–C bond of amorphous C formed by the carbonization process of PVP.

The electrochemical properties of the bare SnS and SnS-C composite powders are shown in Fig. 5. The cyclic voltammogram (CV) curves of the SnS-C composite powders prepared at 900 ˚C from the first to the fifth cycles at a scan rate of 0.1 $mV \cdot s^{-1}$ in the potential range of 0.001–2.0 V are presented in Fig. 5(a). In the first discharge step, a distinctive reduction peak is observed at approximately 0.7 V. This peak can be attributed to the conversion of SnS to Sn metal nanograins and amorphous Na_2S and the formation

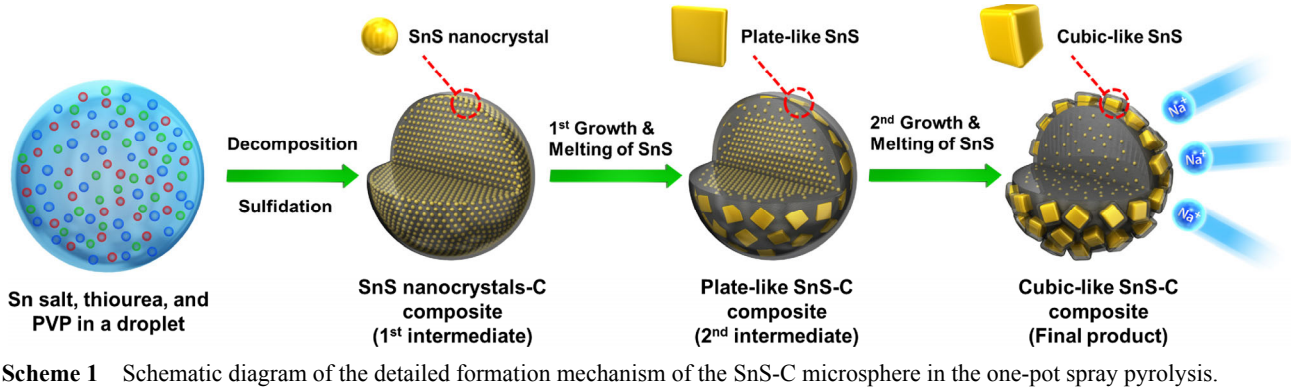

Scheme 1 Schematic diagram of the detailed formation mechanism of the SnS-C microsphere in the one-pot spray pyrolysis.

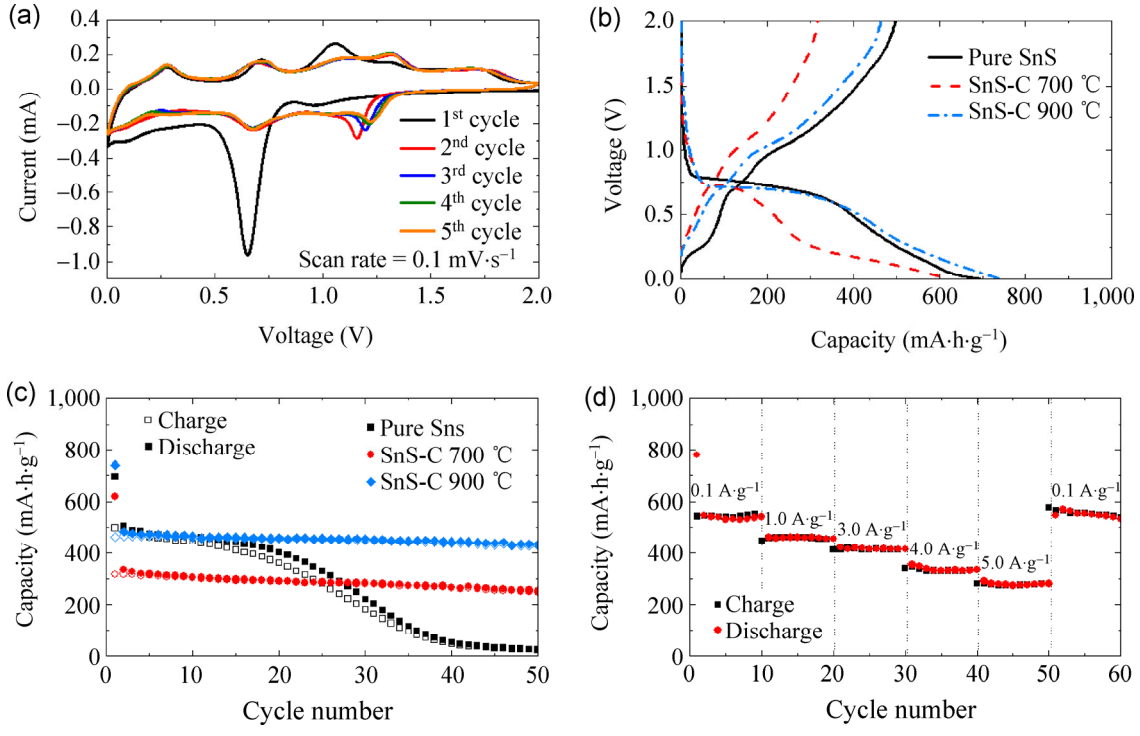

Figure 5 Electrochemical properties of the SnS and SnS-C microspheres: (a) CV curves of SnS-C prepared at 900 ˚C, (b) initial charge/discharge curves at a current density of 0.5 A·g^{-1}, (c) cycling performances at a current density of 0.5 A·g^{-1}, and (d) rate performance.

of a solid electrolyte interface (SEI) layer [33–38]. The broad reduction peak below 0.7 V and the oxidation peaks at 0.28 and 0.72 V are attributed to the formation of Na_xSn alloys and the multi-step dealloying process of Na_xSn to Sn metal, respectively [33–39]. The two oxidation peaks observed at 1.11 and 1.31 V in the CV curves are attributed to the reversible conversion reaction from Sn to SnS [33, 34]. Figure 5(b) presents the initial charge and discharge curves of the powders at a current density of 500 mA·g^{-1}. The bare SnS and SnS-C composite powders prepared at 900 ˚C had long plateaus at approximately 0.7 V resulting mainly from the conversion reaction of SnS to Sn metal nanograins and amorphous Na_2S [33–38]. However, the SnS-C composite powders prepared at 700 ˚C had relatively short plateau at approximately 0.7 V compared with those of the other two samples. The unique structure of the SnS-C composite powders prepared at 700 ˚C changed the shape of the initial discharge curve. The short plateau at approximately 0.7 V resulted from the conversion of the SnS nanoplates, which cover the SnS-C composite microsphere, to Sn metal nanograins. However, the conversion reaction of amorphous SnS located inside the SnS-C composite microsphere resulted in an inclined curve in the voltage range of 0.5–0.01 V in the first discharging process. The distinct plateau resulting from the conversion reaction of SnS is not observed in the second discharging process shown in Fig. S4. The initial discharge capacities of the bare SnS and SnS-C composite powders prepared at 900 ˚C were 695 and 740 mA·h·g^{-1}, respectively, and their initial coulombic efficiencies were 72% and 63%, respectively. In comparison, the SnS-C composite powders prepared at 700 ˚C had lower corresponding values of 618 mA·h·g^{-1} and 51%, respectively. These lower values, compared with those obtained in the materials prepared at 900 ˚C, reflect the effect of a high content of amorphous C with low capacity and high initial irreversible capacity loss. The cycling performances of the bare SnS and SnS-C composite powders at a current density of 500 mA·g^{-1} are shown in Fig. 5(c). The SnS-C composite powders prepared at 700 and 900 ˚C exhibited good cycling performances. However, the discharge capacity of the bare SnS powders decreased after 10 cycles. The 50th discharge capacities and corresponding capacity retentions

measured from the second cycle of the bare SnS and SnS-C composite powders prepared at 900 ℃ were 25 and 433 mA·h·g^{-1} and 5 and 89%, respectively. Figure 5(d) shows the rate performance of the SnS-C composite powders prepared at 900 ℃, in which the current density was increased step-wise from 0.1 to 5 A·g^{-1} and returned to 0.1 A·g^{-1}. Ten cycles were measured for each step to evaluate the rate performance. The SnS-C composite powders exhibited 10th discharge capacities of 541, 455, 415, 333, and 280 mA·h·g^{-1} at current densities of 0.1, 1, 3, 4, and 5 A·g^{-1}, respectively. When the current density was returned to 0.1 A·g^{-1}, the discharge capacity recovered to 540 mA·h·g^{-1}.

Impedance spectra obtained both before and after 50 cycles from the bare SnS and SnS-C composite powders prepared at 900 ℃ are presented in Fig. S5. The Nyquist plots show compressed semicircles in the medium-frequency range of each spectrum, which describe the charge transfer resistances (R_{ct}) for these electrodes [44–46]. The bare SnS and SnS-C composite powders had similar charge transfer resistances before cycling. Both samples exhibited a decrease in the resistances because of the conversion of crystalline SnS into amorphous-like SnS after cycling [47, 48]. However, the SnS-C composite powders exhibited lower charge transfer resistances than those of the bare SnS powders after 50 cycles. The SnS-C composite powders with structural stability during cycling exhibited better cycling performance than the bare SnS powders.

4 Conclusions

In summary, the electrochemical properties of bare SnS and SnS-C composite powders prepared by one-pot spray pyrolysis were compared. The bare SnS powders had cubic-like or plate-like structures. However, Ostwald ripening resulted in uniform attachment of cubic-like SnS nanocrystals, which have an amorphous C coating layer, to the C microspheres. The SnS-C composite powders exhibited higher initial capacities and better cycling performances than those of the bare SnS powders for Na-ion storage. The C content with low reversible capacities of the SnS-C composite powders prepared at 900 ℃ was ~25%. This value could be easily controlled by changing the concentration of the PVP dissolved in the spray solution. In addition, the size of the SnS crystals that were attached to the C microspheres could be controlled by optimizing the preparation conditions such as the temperature, residence time, and reducing atmosphere. The aforementioned findings confirm that SnS-C composite powders prepared by one-pot spray pyrolysis can be applied as an efficient anode material for Na-ion batteries.

Acknowledgements

This work was supported by the National Research Foundation of Korea (NRF) grant funded by the Korea government (MEST) (No. 2012R1A2A2A02046367).

Electronic Supplementary Material: Supplementary material (Schematic diagram of spray pyrolysis process, TG curves, X-ray photoelectron spectroscopy (XPS) spectra, second cycle profiles, and electrochemical impedance spectroscopy (EIS) of the bare SnS and SnS-C composite microspheres) is available in the online version of this article at http://dx.doi.org/10.1007/s12274-014-0648-z.

References

[1] Slater, M. D.; Kim, D.; Lee, E.; Johnson, C. S. Sodium-ion batteries. *Adv. Funct. Mater.* **2013**, *23*, 947–958.

[2] Kim, S. W.; Seo, D. H.; Ma, X. H.; Ceder, G.; Kang, K. Electrode materials for rechargeable sodium-ion batteries: Potential alternatives to current lithium-ion batteries. *Adv. Energy Mater.* **2012**, *2*, 710–721.

[3] Palomares, V.; Serras, P.; Villaluenga, I.; Hueso, K. B.; Carretero-González, J.; Rojo, T. Na-ion batteries, recent advances and present challenges to become low cost energy storage systems. *Energy Environ. Sci.* **2012**, *5*, 5884–5901.

[4] Pan, H. L.; Hu, Y. S.; Chen, L. Q. Room-temperature stationary sodium-ion batteries for large-scale electric energy storage. *Energy Environ. Sci.* **2013**, *6*, 2338–2360.

[5] Ellis, B. L.; Nazar, L. F. Sodium and sodium-ion energy storage batteries. *Curr. Opin. Solid. St. M.* **2012**, *16*, 168–177.

[6] Oszajca, M. F.; Bodnarchuk, M. I.; Kovalenko, M. V. Up and coming precisely engineered colloidal nanoparticles and nanocrystals for Li-ion and Na-ion batteries: Model systems or practical solutions? *Chem. Mater.* **2014**, *26*, 5422–5432.

[7] Dahbi, M.; Yabuuchi, N.; Kubota, K.; Tokiwa, K.; Komaba, S. Negative electrodes for Na-Ion batteries. *Phys. Chem. Chem. Phys.* **2014**, *16*, 15007–15028.

[8] Kim, Y.; Ha, K. H.; Oh, S. M.; Lee, K. T. High-capacity anode materials for sodium-ion batteries. *Chem. Eur. J.* **2014**, *20*, 11980–11992.

[9] Klein, F.; Jache, B.; Bhide, A.; Adelhelm, P. Conversion reactions for sodium-ion batteries. *Phys. Chem. Chem. Phys.* **2013**, *15*, 15876–15887.

[10] Su, D. W.; Ahn, H. J.; Wang, G. X. SnO_2@graphene nanocomposites as anode materials for Na-ion batteries with superior electrochemical performance. *Chem. Commun.* **2013**, *49*, 3131–3133.

[11] Jian, Z. L.; Zhao, B.; Liu, P.; Li, F. J.; Zheng, M. B.; Chen, M. W.; Shi,Y.; Zhou, H. S. Fe_2O_3 nanocrystals anchored onto graphene nanosheets as the anode material for low-cost sodium-ion batteries. *Chem. Commun.* **2014**, *50*, 1215–1217.

[12] Alcántara, R.; Jaraba, M.; Lavela, P.; Tirado, J. L. $NiCo_2O_4$ spinel: First report on atransition metal oxide for the negative electrode of sodium-ion batteries. *Chem. Mater.* **2002**, *14*, 2847–2848.

[13] Jiang, Y. Z.; Hu, M. J.; Zhang, D.; Yuan, T. Z.; Sun, W. P.; Xu, B.; Yan, M. Transition metal oxides for high performance sodium ion battery anodes. *Nano Energy* **2014**, *5*, 60–66.

[14] Rahman, M. M.; Glushenkov, A. M.; Ramireddy, T.; Chen, Y.; Electrochemical investigation of sodium reactivity with nanostructured Co_3O_4 for sodium-ion batteries. *Chem. Commun.* **2014**, *50*, 5057–5060.

[15] Yuan, S.; Huang, X. L.; Ma, D. L.; Wang, H. G.; Meng, F. Z.; Zhang, X. B. Engraving copper foil to give large-scale binder-free porous CuO arrays for a high-performance sodium-ion battery anode. *Adv. Mater.* **2014**, *26*, 2273–2279.

[16] Wang, L. J.; Zhang, K.; Hu, Z.; Duan, W.; Cheng, F. Y.; Chen, J. Porous CuO nanowires as the anode of rechargeable Na-ion batteries. *Nano Res.* **2014**, *7*, 199–208.

[17] Wen, J. W.; Zhang, D. W.; Zang, Y.; Sun, X.; Cheng, B.; Ding, C. X.; Yu, Y.; Chen, C. H. Li and Na storage behavior of bowl-like hollow Co_3O_4 microspheres as an anode material for lithium-ion and sodium-ion batteries. *Electrochim. Acta* **2014**, *132*, 193–199.

[18] Chen, J. S.; Lou, X. W. SnO_2-based nanomaterials: Synthesis and application in lithium-ion batteries. *Small* **2013**, *9*, 1877–1893.

[19] Armstrong, M. J.; O'Dwyer, C.; Macklin, W. J.; Holmes, J. D. Evaluating the performance of nanostructured materials as lithium-ion battery electrodes. *Nano Res.* **2014**, *7*, 1–62.

[20] Wang, Z. Y.; Zhou, L.; Lou, X. W. Metal oxide hollow nanostructures for lithium-ion batteries. *Adv. Mater.* **2012**, *24*, 1903–1911.

[21] Zhou, G. M.; Wang, D. W.; Li, L.; Li, N.; Li, F.; Cheng, H. M. Nanosize SnO_2 confined in the porous shells of carbon cages for kinetically efficient and long-term lithium storage. *Nanoscale* **2013**, *5*, 1576–1582.

[22] Ko, Y. N.; Park, S. B.; Kang, Y. C. Design and fabrication of new nanostructured SnO_2-carbon composite microspheres for fast and stable lithium storage performance. *Small* **2014**,*10*, 3240–3245.

[23] Zhou, X. S.; Wan, L. J.; Guo, Y. G. Binding SnO_2 nanocrystals in nitrogen-doped graphene sheets as anode materials for lithium-ion batteries. *Adv. Mater.* **2013**, *25*, 2152–2157.

[24] Lu, J.; Nan, C. Y.; Li, L. H.; Peng, Q.; Li, Y. D. Flexible SnS nanobelts: Facile synthesis, formation mechanism and application in li-ion batteries. *Nano Res.* **2013**, *6*, 55–64.

[25] Li, L.; Kovalchuk, A.; Tour, J. M. SnO_2-reduced graphene oxide nanoribbons as anodes for lithium ion batteries with enhanced cycling stability. *Nano Res.* **2014**, *7*, 1319–1326.

[26] Cai, J. J.; Li, Z. Z.; Shen, P. K. Porous SnS nanorods/carbon hybrid materials as highly stable and high capacity anode for Li-ion batteries. *ACS Appl. Mater. Interfaces* **2012**, *4*, 4093–4098.

[27] Choi, S. H.; Kang, Y. C. Synthesis for yolk-shell-structured metal sulfi de powders with excellent electrochemical performances for lithium-ion batteries. *Small* **2014**, *10*, 474–478.

[28] Vaughn II, D. D.; Hentz, O. D.; Chen, S.; Wang,D.; Schaak, R. E. Formation of SnS nanoflowers for lithium ion batteries. *Chem. Commun.* **2012**, *48*, 5608–5610.

[29] Luo, B.; Fang, Y.; Wang, B.; Zhou, J. S.; Song, H. H.; Zhi, L. J. Two Dimensional graphene–SnS_2 hybrids with superior rate capability for lithium ion storage. *Energy Environ. Sci.* **2012**, *5*, 5226–5230.

[30] Seo, J.-W.; Jang, J.-T.; Park, S.-W.; Kim, C.; Park, B.; Cheon, J. Two-dimensional SnS_2 nanoplates with extraordinary high discharge capacity for lithium ion batteries. *Adv. Mater.* **2008**, *20*, 4269–4273.

[31] Sathish, M.; Mitani, S.; Tomai, T.; Honma, I. Ultrathin SnS_2 nanoparticles on graphene nanosheets: Synthesis, characterization, and Li-ion storage applications. *J. Phys. Chem. C* **2012**, *116*, 12475−12481.

[32] Pei, L. K.; Jin, Q.; Zhu, Z. Q.; Zhao, Q.; Liang, J.; Chen, J. Ice-templated preparation and sodium storage of ultrasmall SnO_2 nanoparticles embedded in three dimensional graphene. *Nano Res.* **2015**, *8*, 184−192.

[33] Wu, L.; Hu, X. H.; Qian, J. F.; Pei, F.; Wu, F. Y.; Mao, R. J.; Ai, X. P.; Yang, H. X.; Cao, Y. L. A Sn–SnS–C nanocomposite as anode host materials for Na-ion batteries. *J. Mater. Chem. A* **2013**, *1*, 7181–7184.

[34] Zhou,T. F.; Pang,W. K.; Zhang, C. F.; Yang, J. P.; Chen,Z. X.; Liu, H. K.; Guo, Z. P. Enhanced sodium-ion battery perfor-

mance by structural phase transition from two-dimensional hexagonal-SnS_2 to orthorhombic-SnS. *ACS Nano* **2014**, *8*, 8323–8333.

[35] Qu, B. H.; Ma, C. Z.; Ji, G.; Xu, C. H.; Xu, J.; Meng, Y. S.; Wang, T. H.; Lee, J. Y. Layered SnS_2-reduced graphene oxide composite—a high-capacity, high-rate, and long-cycle life sodium-ion battery anode material. *Adv. Mater.* **2014**, *26*, 3854–3859.

[36] Dutta, P. K.; Sen, U. K.; Mitra, S. Excellent electrochemical performance of tin monosulphide (SnS) as a sodium-ion battery anode. *RSC Adv.* **2014**, *4*, 43155–43159.

[37] Xie, X. Q.; Su, D.; Chen, S. Q.; Zhang, J. Q.; Dou, S. X.; Wang, G. X. SnS_2 nanoplatelet@graphene nanocomposites as high-capacity anode materials for sodium-ion batteries. *Chem. Asian J.* **2014**, *9*, 1611–1617.

[38] Prikhodchenko, P. V.; Yu, D. Y. W.; Batabyal, S. K.; Uvarov, V.; Gun, J.; Sladkevich, S.; Mikhaylov, A. A.; Medvedev, A. G.; Lev, O. Nanocrystalline tin disulfide coating of reduced graphene oxide produced by the peroxostannate deposition route for sodium ion battery anodes. *J. Mater. Chem. A* **2014**, *2*, 8431–8437.

[39] Xiao, L. F.; Cao, Y. L.; Xiao, J.; Wang, W.; Kovarik, L.; Nie, Z. M.; Liu, J. High capacity, reversible alloying reactions in SnSb/C nanocomposites for Na-ion battery applications. *Chem. Commun.* **2012**, *48*, 3321–3323.

[40] Choi, S. H.; Boo, S. J.; Lee, J.-H.; Kang, Y. C. Electrochemical properties of tungsten sulfide–carbon composite microspheres prepared by spray pyrolysis. *Sci. Rep.* **2014**, *4*, 5755.

[41] Jang, Y. S.; Kang, Y. C. Facile one-pot synthesis of spherical zinc sulfide–carbon nanocomposite powders with superior electrochemical properties as anode materials for Li-ion batteries. *Phys. Chem. Chem. Phys.* **2013**, *15*, 16437–16441.

[42] Yue, G. H.; Lin, Y. D.; Wen, X.; Wang, L. S.; Chen, Y. Z.; Peng, D. L. Synthesis and characterization of the SnS nanowires via chemical vapor deposition. *Appl. Phys. A* **2012**, *106*, 87–91.

[43] Cai, W.; Hu, J.; Zhao, Y. S.; Yang, H. L.; Wang, J.; Xiang, W. D. Synthesis and characterization of nanoplate-based SnS microflowers via a simple solvothermal process with biomolecule assistance. *Adv. Powder Technol.* **2012**, *23*, 850–854.

[44] Yu, D. Y. W.; Hoster, H. E.; Batabyal, S. K. Bulk antimony sulfide with excellent cycle stability as next-generation anode for lithium-ion batteries. *Sci. Rep.* **2014**, *4*, 4562.

[45] Ruffo, R.; Fathi, R.; Kim, D. J.; Jung, Y. H.; Mari, C. M.; Kim, D. K. Impedance analysis of $Na_{0.44}MnO_2$ positive electrode for reversible sodium batteries in organic electrolyte. *Electrochim. Acta* **2013**, *108*, 575–582.

[46] Choi, S. H.; Kang, Y. C. Yolk–shell, hollow, and single-crystalline $ZnCo_2O_4$ powders: Preparation using a simple one-pot process and application in lithium-ion batteries. *ChemSusChem* **2013**, *6*, 2111–2116.

[47] Su, Q. M.; Du, G. H.; Zhang, J.; Zhong, Y. J.; Xu, B. S.; Yang, Y. H.; Neupane, S.; Li, W. Z. In situ transmission electron microscopy observation of electrochemical sodiation of individual Co_9S_8-filled carbon nanotubes. *ACS Nano* **2014**, *8*, 3620–3627.

[48] Choi, S. H.; Kang, Y. C. Fe_3O_4-decorated hollow graphene balls prepared by spray pyrolysis process for ultrafast and long cycle-life lithium ion batteries. *Carbon* **2014**, *79*, 58–66.